We are IntechOpen, the world's leading publisher of Open Access books
Built by scientists, for scientists

5,300
Open access books available

130,000
International authors and editors

155M
Downloads

154
Countries delivered to

Our authors are among the

TOP 1%
most cited scientists

12.2%
Contributors from top 500 universities

BOOK CITATION INDEX
CLARIVATE ANALYTICS
INDEXED

WEB OF SCIENCE™

Selection of our books indexed in the Book Citation Index
in Web of Science™ Core Collection (BKCI)

Interested in publishing with us?
Contact book.department@intechopen.com

Numbers displayed above are based on latest data collected.
For more information visit www.intechopen.com

Turbulent Flow Fluid in the Hydrodynamic Plain Bearing to a Non-Textured and Textured Surface

Bendaoud Nadia and Mehala Kadda

Abstract

Hydrodynamic bearing are components that provide the guiding in rotation of rotating machines, such as turbines, the reactors. This equipment works under very severe operating conditions: high rotational speed and high radial load. In order to improve the hydrodynamic performance of these rotating machines, the industrialists specialized in the manufacture of hydrodynamic journal bearings, have designed a bearing model with its textured interior surface. The present work is a numerical analysis, carried out to observe the effect of a turbulent fluid flow in a non-textured and textured plain bearing and to thus to see the improvement of the hydrodynamic and tribological performances to a non- textured and textured surface of the plain bearing, under severe operating parameters. The rotational velocity varies from 11,000 to 21,000 rpm and radial load ranging from 2000 N to 9000 N. The numerical analysis is performed by solving the continuity equation of Navier-Stocks, using the finite volume method. The numerical results show that the most important hydrodynamic characteristics such as pressure, flow velocity of the fluid, friction torque, are significant for the textured plain bearing under rotational velocity of 21,000 rpm and radial load 10,000 N compared to obtained for a non-textured plain bearing.

Keywords: plain bearing, turbulent flow fluid, textured surface, pressure, friction torque

1. Introduction

Tribology is the science that studies the interactions of two surfaces in motion with respect to each other. It encompasses the associated technique and all of the friction and wear sectors, including lubrication. She studies the interactions between contact surfaces, but also those of solids, liquids and gases present between these surfaces, such as hydrodynamic plain bearings.

The hydrodynamic bearings allow the various parts of the mechanical devices to move easily while ensuring reliability that eliminates any risk of rupture or premature wear. When the operating conditions are severe (high or rapidly changing loads, high frequency of rotation), working under a turbulent regime (like the turbojet), it becomes difficult to achieve this double objective without the help of powerful digital prediction models.

Friction is one of the most answered physical phenomena in hydrodynamic bearings. This is the reason why a new concept of bearings was invented, the aim of which is to minimize the losses of material and energy linked to wear and friction; it is therefore to manufacture mechanical systems with textured surfaces to improve the efficiency and life of the machines. The aim of this study is to better predict the effect of tribological behavior as well as the effect of turbulent flow behavior in the textured and non-textured hydrodynamic bearing.

2. Turbulent flow effect in plain bearing

Constantinescu has developed the phenomenon of turbulence in lubrication between years 1962 and 1965 [1, 2], Elrod and Ng in 1967 [3–5], are presented a linearized turbulent lubrication theory based on eddy-viscosity concept of Boussinesq and Reichardt's formulation, including the treatment of turbulent shear and pressure gradient flows in thin films. This theory can be applied to the journal bearings by assuming that the turbulent flow field in the clearance space can be represented by the small perturbations on the turbulent Couette flow. The first studies on determining the Reynolds number, which expresses the ratio, changed inertial forces and viscous forces in the field of bearings, were made by Fantinos and colleagues [6].

In 2005 Braunetiere [7], show that a number of theories for the turbulent lubrication film exist which are based on various well-established models of turbulent flow. Solghar and Nassab (2013) [8] carry out a study in to assess the turbulent thermohydrodynamic (THD) performance characteristics of an axially grooved finite journal bearing [8, 9]. They are mentioned in their research that the bearing of the operating characteristics are significantly changed by increasing the Reynolds number.

3. Texture effect in plain bearing

At the moment, little is known about the effect of variations in the profile of the bushing and on its performance. Surface texturing is expected to make a significant contribution to future bearing technologies.

In 2011, Ivan Krupka and al [10] presents an experimental and numerical study on the superficial textures effect of the lubricated contact, for the transitional phase. This study is done in order to observe the lubricant film behavior between two surfaces of a disc coated with chrome and a steel ball. According to their study, they showed that lubricant produced from the micro-dents helps to separate rubbing surfaces.

Tala-Ighil, Fillon and Maspeyrot in 2011 [11] indicated the effect of textured area on the performances of a hydrodynamic journal bearing. They examined the texture location effect on the hydrodynamic performance hydrodynamic of the journal bearing. Their results show that the most important characteristics can be improved through an appropriate arrangement of the textured area on the contact surface.

In 2014, Pratibha and Chandreshkumar [12], present an experimental study on the effect of the bearing surface texture and the profile pressure distribution in hydrodynamic performance of journal bearing. Their study shows that with the increase of the radial loads and at the constant velocity, the increase of maximum pressure is significant in textured journal bearing, in contrast, this pressure is less important for a non-textured journal bearing and with the increase of velocity and at constant radial load.

In 2015 Zhang and al [13], present a numerical study of surface texturing for improving tribological properties of ultra-high molecular weight polyethylene. Ultra-high molecular weight polyethylene (UHMWPE). Smooth UHMWPE surfaces are used for total joint replacements; however, smooth surface contacts have been shown to be inadequate in friction reduction and/or anti-wear.

Uddin and Liu present in 2016 [14], present design and optimization of a texture shape (star-like) for to improve the tribological performance. The triangle form of the texture tends to reducing the friction. A star-like texture consisting of a series of triangular pikes is positioned around the texture center's proposed. The increasing theses triangular shape, produce the increases the film pressure and on the other hand the reduction of the friction.

In 2016, Shahab Hamdavi, H. H. Ya and T. V. V. L. N. Rao [15], presented a research on the surface texturing effect on hydrodynamic performance of journal bearings. The authors study the effect of partially textured surface of long journal bearing on the pressure distribution. The results show that, applying partial surface texture has a positive and remarkable effect on operating characteristics of the bearings.

In 2017, Sedlaček and al [16], studied the geometry effect and the sequence of the surface texturing process in contact on the tribological characteristics. They tested the behavior of surfaces with and without hard coating for different textures shapes: pyramid, cone and concave. The authors have shown that pyramidal textures cause significant results for tribological behavior. Deposition of textured surface coating tends to reduce friction over that achieved for uncoated textured surface.

Wang et al. presented the study in 2018 [17] on lubrication performance of journal bearing with multiple texture distributions. They are able to compare two shaped concave textures and convex texture on a bearing lubrication performance. Their results show that the bearing load capacity is reduced by the concave spherical texture, but enhanced by the convex texture; both the concave and convex textures have a very slight influence on the friction coefficient. In the same year, Ji and Guan [18], analyses the effect of the micro-dimples on hydrodynamic lubrication of textured sinusoidal surfaces and rough surfaces. In order to characterize the non-textured surfaces, sinusoidal waves were used. Their results show that, the effect of roughness of the textured surface on the hydrodynamic pressure is significant and the load carrying capacity decreases with the increase of the roughness ratio because the roughness greatly suppresses the hydrodynamic effect of dimples.

In 2019, Manser et al. [19] studied the hydrodynamic journal bearing performance under the combined influence of textured surface and journal misalignment. This study is a numerical analysis is performed to test three texture shapes: square "SQ," cylindrical "CY," and triangular "TR," and shaft misalignment variation in angle and degree. The Reynolds equation of a thin viscous film is solved using the finite difference's method. Their results show that the micro-step bearing mechanism is a key parameter, where the micro-pressure recovery action present in dimples located at the second angular part of the bearing (from 180° to 360°) can compensate for the loss on performances caused by shaft misalignment, while the micro-pressure drop effect at the full film region causes poor performances.

4. Theoretical analysis

The pressure field is determined by the resolution of the generalized Navier-Stokes equation according to the classical assumptions in the $(O, \overset{\cdot}{\theta} \rightarrow, z)$ coordinate system. **Figure 1** illustrates the schematization of plain cylindrical journal bearing.

4.1 Equation fluid flow

4.1.1 Equation of continuity

The continuity equation can be expressed by the relationship (1) [20].

$$\nabla\left(\rho \, \vec{U}\right) = \vec{0} \tag{1}$$

where $\vec{U} = \vec{U}(u, \text{v}, w)$ is the velocity vector.
Eq. (1) can also be written as follows:

$$\frac{\partial u}{\partial x} + \frac{\partial v}{\partial y} + \frac{\partial w}{\partial z} = 0 \tag{2}$$

4.1.2 Navier-Stokes equations

The Navier-Stokes equation can be defined in the following form (2003):

$$\partial\nabla.\left(\vec{U}\otimes\vec{U}\right) = -\nabla p + \mu\nabla.\left(\nabla\vec{U} + \left(\nabla\vec{U}\right)^{T}\right) + B \tag{3}$$

With P static pressure (thermodynamic); U velocity; μ dynamic viscosity.
For fluids in a rotating frame with constant angular velocity ω source term B can be written as follows:

$$B = -\rho \left(2\,\vec{\omega}\times\vec{U} + \vec{\omega}\times\left(\vec{\omega}\times\vec{r}\right)\right) \tag{4}$$

Eq. (1) can also be expressed in the form:

$$\rho\left(u\frac{\partial u}{\partial x} + v\frac{\partial u}{\partial y} + w\frac{\partial u}{\partial z}\right) = -\frac{\partial p}{\partial x} + \mu\left(\frac{\partial^2 u}{\partial x^2} + \frac{\partial^2 u}{\partial y^2} + \frac{\partial^2 u}{\partial z^2}\right) + B_x$$
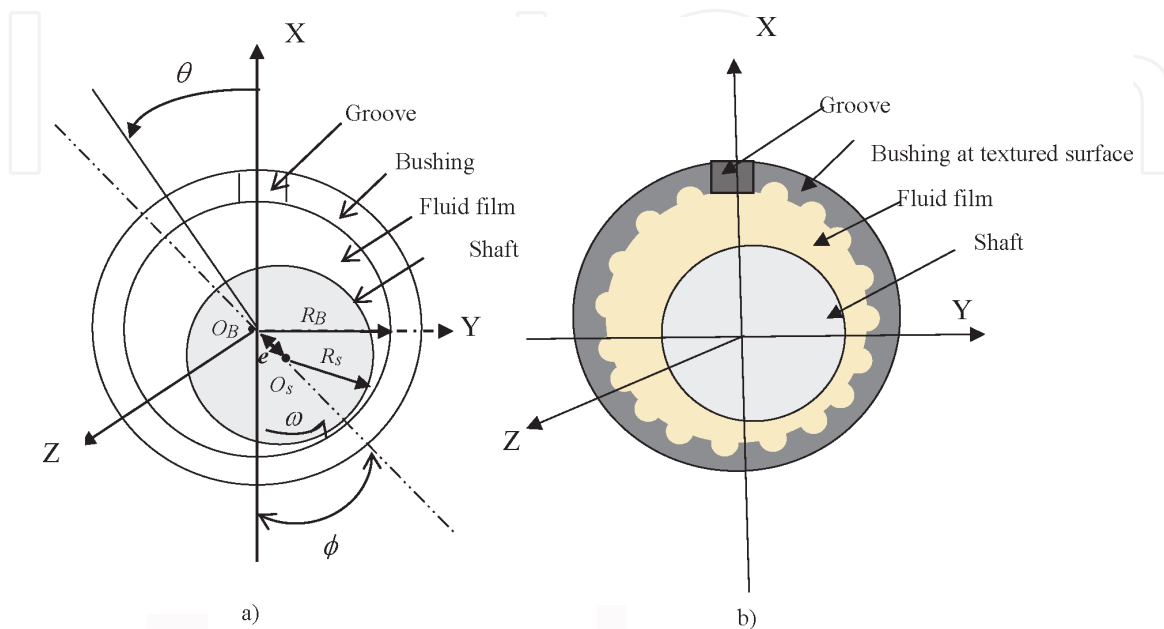

Figure 1.
Schematization of plain bearing. (a) Non-textured plain bearing. (b) Textured plain bearing.

$$\rho\left(u\frac{\partial v}{\partial x} + v\frac{\partial v}{\partial y} + w\frac{\partial v}{\partial z}\right) = -\frac{\partial p}{\partial y} + \mu\left(\frac{\partial^2 v}{\partial x^2} + \frac{\partial^2 v}{\partial y^2} + \frac{\partial^2 v}{\partial z^2}\right) + B_y$$

$$\rho\left(u\frac{\partial w}{\partial x} + v\frac{\partial w}{\partial y} + w\frac{\partial w}{\partial z}\right) = -\frac{\partial p}{\partial z} + \mu\left(\frac{\partial^2 w}{\partial x^2} + \frac{\partial^2 w}{\partial y^2} + \frac{\partial^2 w}{\partial z^2}\right) + B_z$$

(5)

ρ is fluid density.

Considering the Z axis as the axis of rotation, the components of B can be expressed as follows:

$$B_x = \left(\omega_Z^2\, r_x + 2\omega_z v\right)$$

$$B_y = \left(\omega_Z^2\, r_y + 2\omega_z u\right)$$

$$B_z = 0$$

The finite volume method used to solve the continuity and Navier-Stokes equations consists in subdividing the physical domain of the flow into elements of more or less regular volumes; it converts the general differential equation into a system of Algebraic equations by relating the values of the variable under consideration to the adjacent nodal points of a typical control volume. This is achieved by integrating the governing differential equation into this control volume.

4.1.3 Discretization of governance equations

The main step of the finite volume method is the integration of governing equations for each control volume [20]. The algebraic equations deduced from this integration make the resolution of the transport equations simpler. Each node is surrounded by a set of surfaces that has a volume element. All the variables of the problem and the properties of the fluid are stored at the nodes of this element.

The equations governing the flow are presented in their averaged forms in a Cartesian coordinate system (x, y, z):

$$\frac{\partial}{\partial X_j}\left(\rho\, U_j\right) = 0$$

(6)

$$\frac{\partial}{\partial X_j}\left(\rho\, U_j U_i\right) = -\frac{\partial P}{\partial X_i} + \frac{\partial}{\partial X_j}\left(\mu\left(\frac{\partial U_i}{\partial X_i} + \frac{\partial U_j}{\partial X_i}\right)\right) + B_x$$

(7)

Eqs. (6) and (7) can be integrated into a control volume, using the Gaussian divergence theorem to convert volume integrals to surface integrals as follows:

$$\int_s \rho\, U_j dn_j = 0$$

(8)

$$\int_s \rho\, U_j U_i dn_j = -\int_s P\, dn_j + \int_s \left(\mu\left(\frac{\partial U_i}{\partial X_j} + \frac{\partial U_j}{\partial X_i}\right)\right) dn_j + \int_V S_{ui} dv$$

(9)

The next step is to discretize the known m's of the problem as well as the differential operators of this equation. All these mathematical operations will lead to obtaining, on each volume of control, a discretized equation that will link the variables of a cell to those of neighboring cells. All of these discretized equations will eventually form a matrix system. Considering an element of an isolated mesh, **Figure 2**.
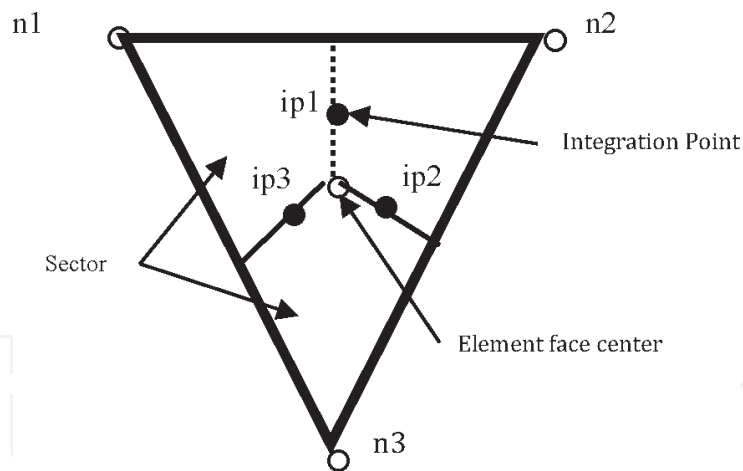
Figure 2.
Integration point in an element of a control volume control.

After the discretization and rearrangement of Eqs. (8) and (9) the following forms will be obtained:

$$\sum_{ip} \left(\rho \, U_j \, \Delta n_j \right)_{ip} = 0 \tag{10}$$

$$\sum_{ip} m_{ip} \, (U_i)_{ip} = \sum_{ip} (P \, \Delta n_j)_{ip} + \sum_{ip} \left(\mu \left(\frac{\partial U_i}{\partial X_j} + \frac{\partial U_j}{\partial X_i} \right) \Delta n_j \right) + \overline{S_{u_i} V} \tag{11}$$

$$N_j = \left\{ \begin{matrix} 1 & i = j \\ 0 & i \neq j \end{matrix} \right\}$$

4.1.4 Coupling pressure-velocity

The method of pressure interpolation in pressure-velocity coupling is similar to that used by Rhie and Chow (1982). This method is among the methods that best save memory space and computation time. If the pressure is known, the discretized equations are easily solved [20]:

$$\left(\frac{\partial U}{\partial x} \right)_i + \frac{\Delta x^3 A}{4m} \left(\frac{\partial^4 P}{\partial x^4} \right) 0 \tag{12}$$

where:

$$m = \rho \, U_i \, \Delta n_j \tag{13}$$

4.1.5 Form functions

The physical quantity ϕ (p, u, v, w and p) of the flow in a volume element is a function of those in the nodes of the element is given by the following relation:

$$\phi = \sum_{i=1}^{Node} N_i \, \phi_i \tag{14}$$

where N_i is the form function for node i and ϕ_i the value of the variable in the same node. A particularity of the form factors makes sure that:

$$\phi = \sum_{i=1}^{\text{Node}} N_i = 1 \qquad (15)$$

These functions are also us5ed for the calculation of various geometric quantities, such as positions, coordinates of the integration point (ip), surfaces and different vectors. Form equations are also applicable for Cartesian coordinates, in which case they can be written in the following way:

$$x = \sum_{i=1}^{\text{Node}} N_i \, x_i \qquad (16)$$

$$y = \sum_{i=1}^{\text{Node}} N_i \, y_i \qquad (17)$$

$$z = \sum_{i=1}^{\text{Node}} N_i \, z_i \qquad (18)$$

The shape functions are also used to evaluate the partial derivatives of the flow terms on the control surfaces and for each direction, the general formula of the different flows is as follows:

$$\left.\frac{\partial \phi}{\partial x}\right|_i = \sum_n \left.\frac{\partial N_n}{\partial x}\right|_{ip} \phi_n \qquad (19)$$

4.1.6 Pressure gradients

The integration of the pressure gradient (P) on the control volume in the Navier-Stokes equations involves the evaluation of the following expression:

$$\left(P \, \Delta n_{ip}\right)_{ip} \qquad (20)$$

where:

$$P_{ip} = \sum_n N_n \left(S_{ip}, t_{ip}, u_{ip}\right) P_n \qquad (21)$$

For the improved treatment of fluctuations induced by turbulence in the motion of a particle of fluid, there are three methods of approach to address the notion turbulence. The first method is to decompose the field of velocity and temperature in a mean component and a turbulent fluctuation, to make a variety of models are now available, ranging from the simple model equation to zero to complex (model of the constraint equations Reynolds RMS).

The second is a method in which all the structures of turbulence (macro and micro-structures) are solved directly and models the effect of small structures by models more or less simple, so-called sub-grid models. This method is known as the large eddy simulation (Large Eddy Simulation, LES). The third method is a hybrid approach combines the advantages qm large eddy simulation (LES), with good results in highly separated zones, and model Reynolds-Averaged Navier-Stokes (RANS), which are most effective in areas close to the walls. The method is called (Detached Eddy Simulation, DES).

5. k-Epsilon model

One of the most prominent turbulence models, the (k-epsilon) model, has been implemented in most CFD codes [20]. It has proven to be stable and numerically robust and has a well-established regime of predictive capability; the model offers a good compromise in terms of accuracy and robustness. This turbulence model uses the scalable wall-function approach to improve robustness and accuracy when the near-wall mesh is very fine.

k is the turbulence kinetic energy and is defined as the variance of the fluctuations in velocity. It has dimensions of ($L^2 T^{-2}$); for example, m²/s². ε is the turbulence eddy dissipation (the rate at which the velocity fluctuations dissipate), and has dimensions of k per unit time ($L^2 T^{-3}$); for example, m²/s³.

The k-ε model introduces two new variables into the system of equations. The continuity equation is following forms:

$$\frac{\partial \rho}{\partial t} + \frac{\partial}{\partial x_j}\left(\rho\, U_j\right) = 0 \tag{22}$$

and the momentum equation becomes:

$$\frac{\partial \rho\, U_i}{\partial t} + \frac{\partial}{\partial x_j}\left(\rho\, U_i U_j\right) = -\frac{\partial p'}{\partial x_i} + \frac{\partial}{\partial x_j}\left[\mu_{\text{eff}}\left(\frac{\partial U_i}{\partial x_j} + \frac{\partial U_j}{\partial x_i}\right)\right] + S_M \tag{23}$$

where S_M is the sum of body forces, μ_{eff} is the effective viscosity accounting for turbulence, and p' is the modified pressure as defined in Eq. (22).

$$p' = p + \frac{2}{3}\,\rho\, k + \frac{2}{3}\,\mu_{\text{eff}}\,\frac{\partial U_k}{\partial x_k} \tag{24}$$

The k-ε model, like the zero equation model, is based on the eddy viscosity concept, so that:

$$\mu_{\text{eff}} = \mu + \mu_t \tag{25}$$

where μ_t is the turbulence viscosity. The k-ε model assumes that the turbulence viscosity is linked to the turbulence kinetic energy and dissipation:

$$\mu_t = C_\mu \rho\, \frac{k^2}{\varepsilon} \tag{26}$$

where $C\mu$ is a constant.

With $C_\mu = 0.09\ \theta = k^{1/2}\ l = \frac{k^{3/2}}{\varepsilon}$.

The values of k and ε come directly from the differential transport equations for the turbulence kinetic energy and turbulence dissipation rate:

$$\frac{\partial(\rho\, k)}{\partial t} + \frac{\partial}{\partial x_j}\left(\rho\, U_j k\right) = \frac{\partial}{\partial x_j}\left[\left(\mu + \frac{\mu_t}{\sigma_k}\right)\frac{\partial k}{\partial x_j}\right] + P_k - \rho\,\varepsilon + P_{\text{kb}} \tag{27}$$

$$\frac{\partial(\rho\, \varepsilon)}{\partial t} + \frac{\partial}{\partial x_j}\left(\rho\, U_j \varepsilon\right) = \frac{\partial}{\partial x_j}\left[\left(\mu + \frac{\mu_t}{\sigma_\varepsilon}\right)\frac{\partial \varepsilon}{\partial x_j}\right] + \frac{\varepsilon}{k}\left(C_{\varepsilon 1}P_k - C_{\varepsilon 2}\,\rho\,\varepsilon + C_{\varepsilon 1}P_{\text{kb}}\right) \tag{28}$$

where $C_{\varepsilon 1}$, $C_{\varepsilon 2}$, σ_k and σ_ε are constants.

P_{kb} and $P_{\varepsilon b}$ represent the influence of the buoyancy forces, which are described below. P_k is the turbulence production due to viscous forces, which is modeled using:

$$P_k = \mu_t \left(\frac{\partial U_i}{\partial x_j} + \frac{\partial U_j}{\partial x_i} \right) \frac{\partial U_i}{\partial x_j} - \frac{2}{3} \frac{\partial U_k}{\partial x_k} \left(3\mu_t \frac{\partial U_k}{\partial x_k} + \rho\, k \right) \tag{29}$$

The term $3\mu_t$ in Eq. (37) is based on the "frozen stress" assumption. This prevents the values of k and ε becoming too large through shocks.

6. Numerical model

The purpose of this study is to highlight the behavior of the turbulent fluid flow fluid on the operating characteristics as well as the hydrodynamic behavior of a plain bearing This study is simulated by the CFD calculation code, which provides accuracy, reliability, speed and flexibility in potentially complex flow areas. Integrating the Reynolds equation on each control volume to derive an equation connecting the discrete variables of the elements that surround it, all of these equations eventually form a matrix system.

6.1 3D structure of the numerical model

Figure 3 illustrates the 3-D structure of the plain bearing with fluid and solid regions are shown. The supply holes are presented in a simplified manner without affecting the accuracy of the model. A tetrahedron element is adopted in the oil supply holes of the fluid region, and a hexahedral element is adopted in domain fluid. A hexahedral element is also applied to the solid region such as the bearing and the shaft (**Figure 4**).

The geometrical and operating parameters of the plain journal bearing is presented in the **Table 1**. As well as, parameters of the lubricant are showed in **Table 2**.

6.2 Boundary conditions of the numerical model

Boundary conditions of the numerical model of the plain bearing are shown in **Figure 5**, definite as follows: 1: the rotating speed is applied to the outer wall surface
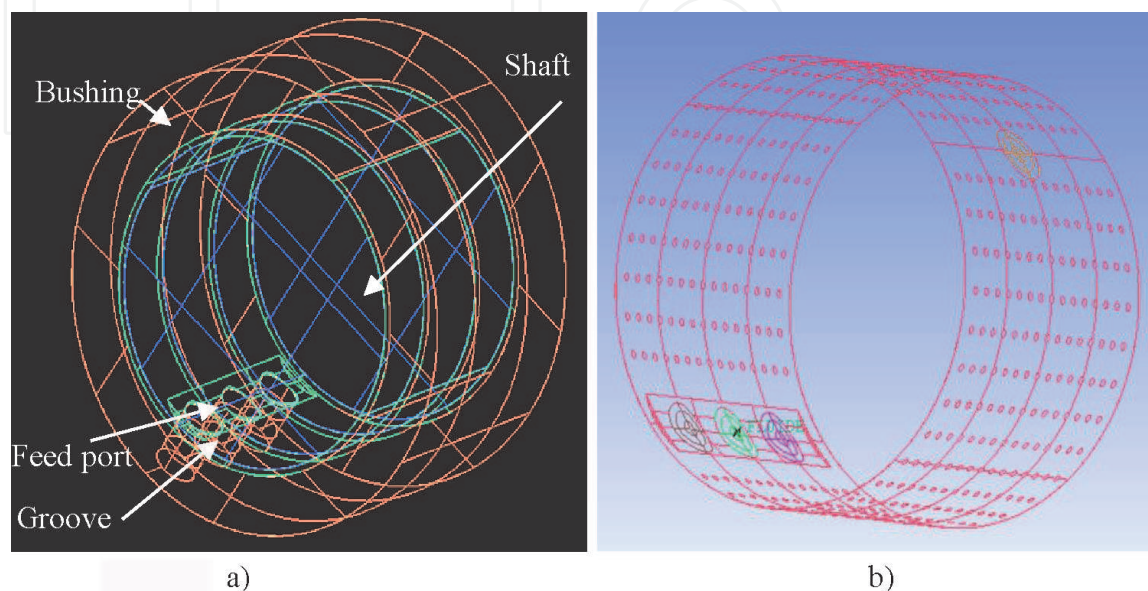

a)   b)

Figure 3.
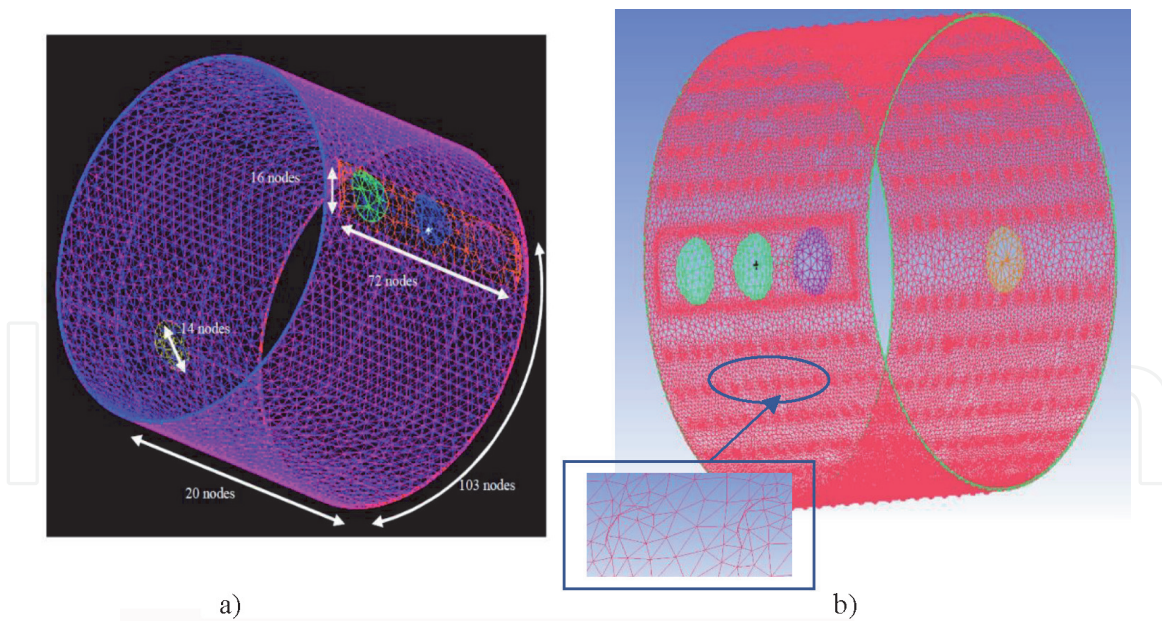*3D structure of the non-textured plain bearing. (a) Non-textured bearing. (b) textured bearing.*

Figure 4.
Mesh of the plain bearing. (a) Non-textured bearing. (b) textured bearing.

Item	Value
Bearing diameter (mm)	100
Shaft diameter (mm)	99.91
Bearing length (mm)	70
Radial clearance (mm)	0.09
Pad thickness (mm)	4
Feed port diameter (mm)	14
Feed groove length (mm)	70
Rotating velocity N (rpm)	11,000–- 21, 000
Radial load W (N)	2000–20- 10, 000
Supply temperature ambiaente Ta (°C)	40
Supply pressure Pa (MPa)	0.08

Table 1.
Geometrical and operating parameters of the plain bearing.

Item	Value
Lubricant type	PMA3
Density ρ (kg/m^3)	800
Specific heat capacity C (J/kg. K)	2000
Kinematic viscosity at 40 °C υ_1 (mm^2/s)	17.,49
Kinematic viscosity at 80 °C υ_2 (mm^2/s)	8,003

Table 2.
Parameters of the lubricant.

of the shaft; 2: the inner wall surface of the bushing is stationary; 3: the domain is simulated by the fluid region. The slip of the interface is ignored; 4: the oil supply pressure is 0.08 MPa and supply temperature is 40°C, are set in oil supply holes;
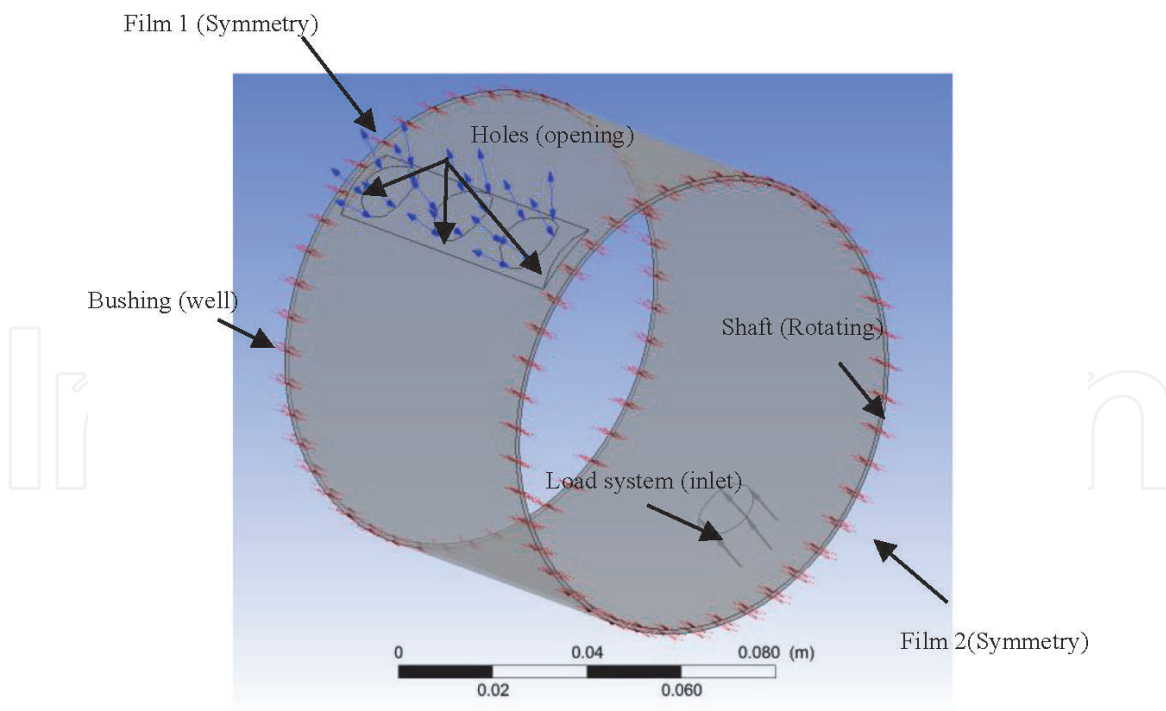
Figure 5.
Boundary conditions.

5: the two ends of the plain bearing domain, and the pressure is set to one bar; and is considered as symmetry.

6.3 Validation of the mesh independence of the numerical model

The setting is done by a graphical interface. The mesh used is a mixed mesh which understood elements of tetrahedral type with 6 nodes and hexahedral elements with 8 nodes. It's necessary to choose an appropriate mesh, consequently, a mesh independence study is carried out, and calculation results are shown in **Figure 6**. When the nodes number is greater than 4815, the evolution of the pressure stabilizes in the angular coordinate 205° of the plain bearing. Therefore, the number of nodes chosen for this numerical analysis corresponds to a number of nodes equal to 4815. The nodes number for textured bearing is 65,172. Convergence criterion of the numerical results is calculated for a maximum number of iterations
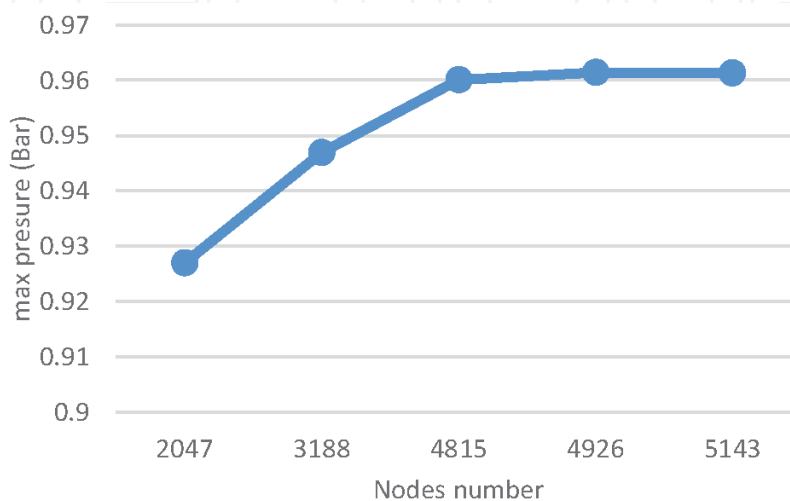
Figure 6.
Evolution max pressure according to the nodes number of the shaft mesh.
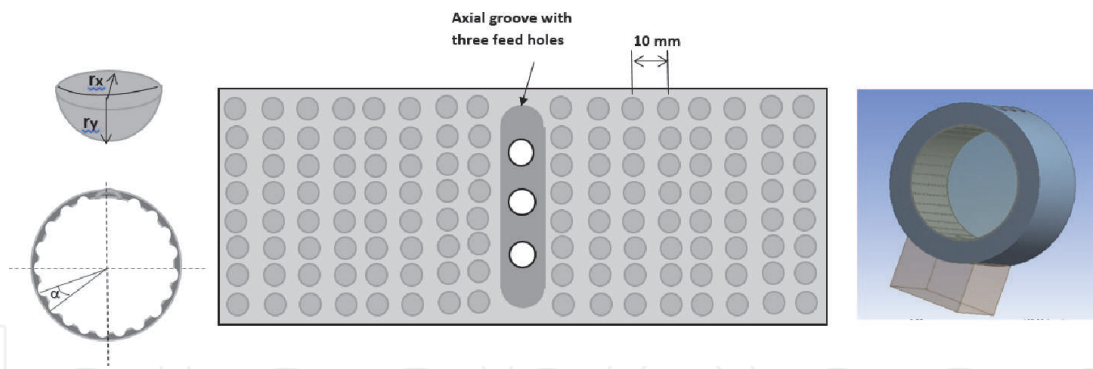
Figure 7.
Textured bushing parameters.

of 1000 iterations with a convergence criterion of the order of 10^{-4}. The solution converges when the residuals reach 10^{-4}. However, in some cases it is necessary to push the calculations to 10^{-6}.

6.4 Textures parameters

Surface texturing of the bushing is a technique used to improve the load capacity of various tribological conjunctions, as well as to reduce frictional losses. The texture spherical shape of diameter r_x = 3 mm and the depth of r_y = 0.5 mm, the axial distance between the textures d = 10 mm and their angular offsets α = 10°, (**Figure 7**).

7. Hydrodynamic and tribological performance of a hydrodynamic non-textured and textured plain bearing for the turbulent regime

7.1 Test of the different turbulent model

In this section, we will carry out a comparative study between two models of turbulence: k-ε model for turbulence in the vicinity of the walls and the RMS model (Reynolds shear stress) for turbulence in the vicinity and far from the walls. **Figure 8** illustrates the pressure distribution along the median plane of the plain bearing, for the k-ε model and the RMS model. Both models give the same pressure distribution. Since we are interested in examining the distribution of pressure, of

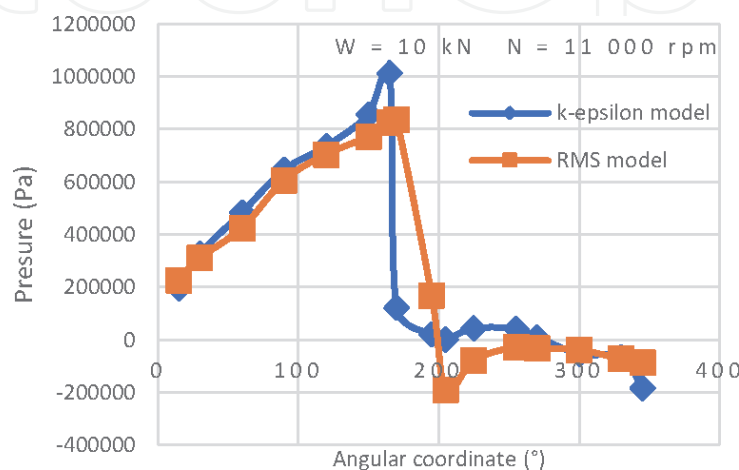**Figure 8.**
Pressure evolution for k-epsilon model and Reynolds shear stress (RMS).

the friction torque between the fluid and the internal surface of the bearing, we used the k-ε model for the numerical analysis carried out in this study.

7.2 Radial load effect

To demonstrate the effect of the radial load on the operating performance of the non-textured and textured hydrodynamic plain bearing, such as pressure, fluid flow velocity and friction torque, the radial load is varied (W1 = 2000 N, W2 = 5000 N, W3 = 7000 N and W3 = 9000 N). The initial operating conditions of the bearing re a supply temperature Ta = 40° C, supply pressure Pa = 0.08 MPa and the rotational speed of the shaft equal to 11,000 rpm with a Reynolds number of Re = 3622.64 to ensure the turbulent regime.

7.2.1 Pressure

Figure 9 illustrates the distribution of the pressure along the median plane for non-textured and textured bearing, for different radial loads. The graph shows that increasing the load from 2000 N to 9000 N leads to an increase in pressure. Significant pressures are obtained for a bearing subjected to a radial load of 9000 N. This increase reaches 65 per cent for a textured bearing. Also for a no textured bearing, the increase in pressure will reach 81 per cent by varying the radial load from 2kN to 9kN. The curves also indicate that the maximum pressure is noted in the angular position from 160° to 175°, on the other hand, in the angular coordinates at 200°, the noted pressure is lower than the supply pressure, indicating the existence rupture zones of the oil film. The rupture zones of the oil film are observed in the angular positions between 190° and 335° and also between 300° and 350°. The values of circumferential pressure are significant for a textured bearing with respect to those recorded for a non-textured bearing (**Figure 10**).

7.2.2 Fluid flow velocity

The fluid flow velocity according to the angular position of the plain bearing, for different radial loads is presented in **Figure 11**. The maximum flow velocity is noted for a textured plain bearing working under a radial load of 9000 N and which is of the order of 61 m/s, on the other hand is of the order of 36 m/s for non-textured plain bearing. The increase in the radial load which reacts on the bearing causes the increase in the flow velocity. This increase is estimated at 21
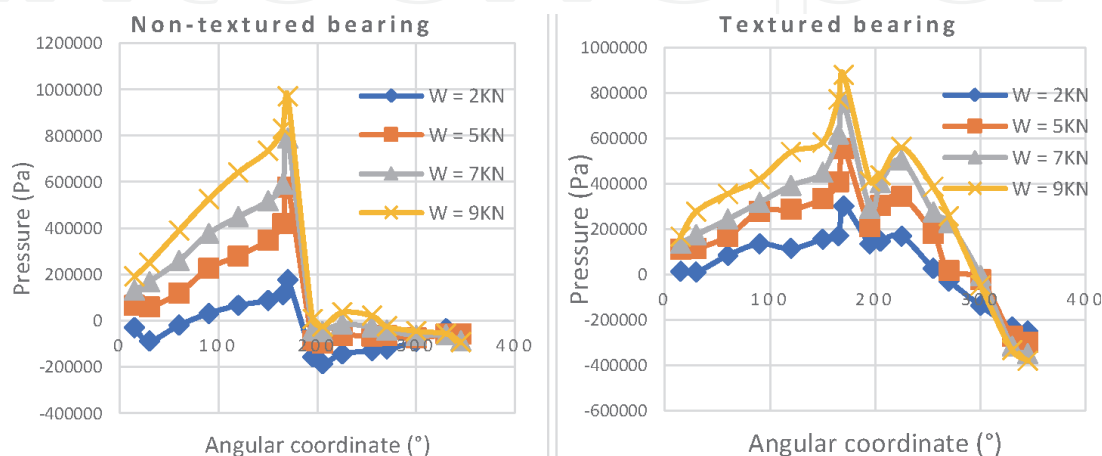

Figure 9.
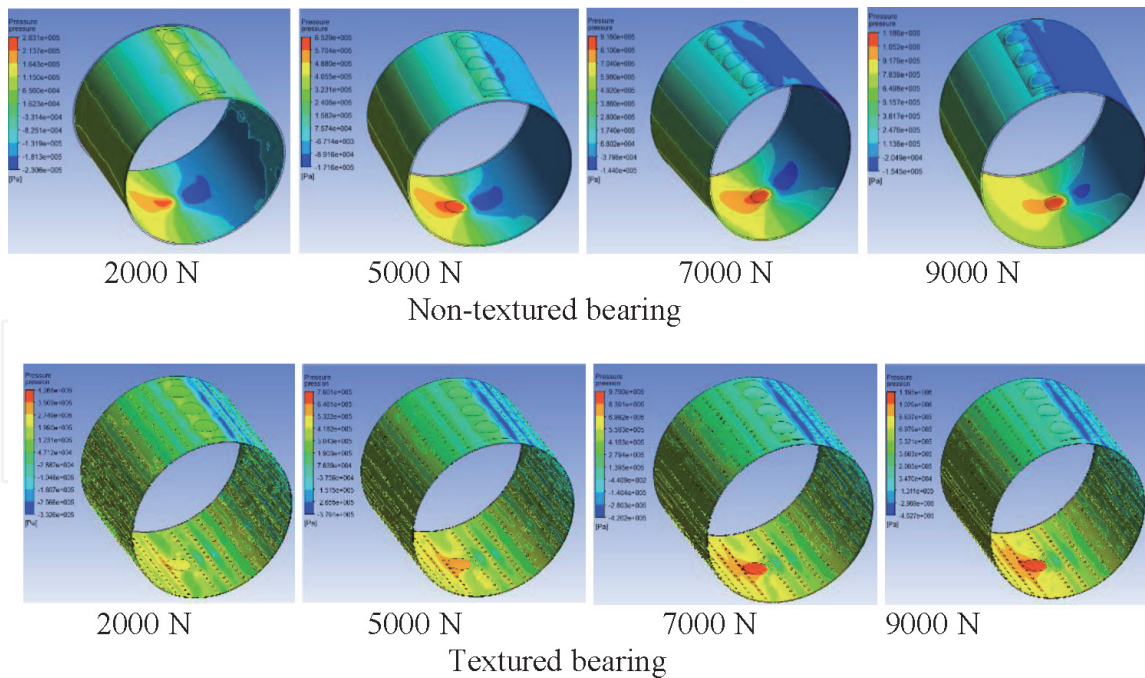*Circumferential pressure for different radial load N = 11,000 rpm (Re = 3622.64 turbulent regime).*

2000 N   5000 N   7000 N   9000 N

Non-textured bearing

2000 N   5000 N   7000 N   9000 N

Textured bearing

Figure 10.
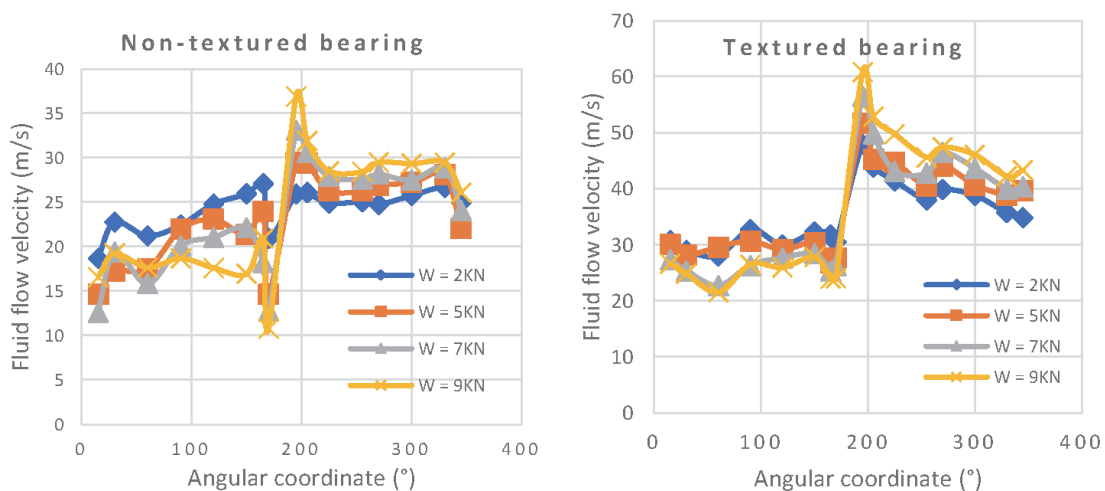*Pressure evolution for different radial load N = 11,000 rpm.*

Figure 11.
Evolution of the fluid flow velocity according the angular position for different radial load N = 11,000 rpm (Re = 3622.64 turbulent regime).

per cent for textured bearing and estimated at 29 per cent for non-textured bearing (**Figure 12**).

7.2.3 Friction torque

The fluid friction torque or "viscous" friction is a particular friction force, which is associated with the movement of an object in a fluid (air, water, etc.). It is at the origin of energy losses by friction for the object moving in the fluid. The friction torque is calculated by integrating the shear stresses at the surface of the shaft or of the bushing, the shear stresses in the fluid are given by derivation the fluid velocity in the radial and tangential direction. Therefore, there is an empirical relationship between the flow velocity of the fluid and the friction torque, for this we obtain the same distribution for the fluid flow velocity and the friction torque along the median plane of the hydrodynamic bearing.
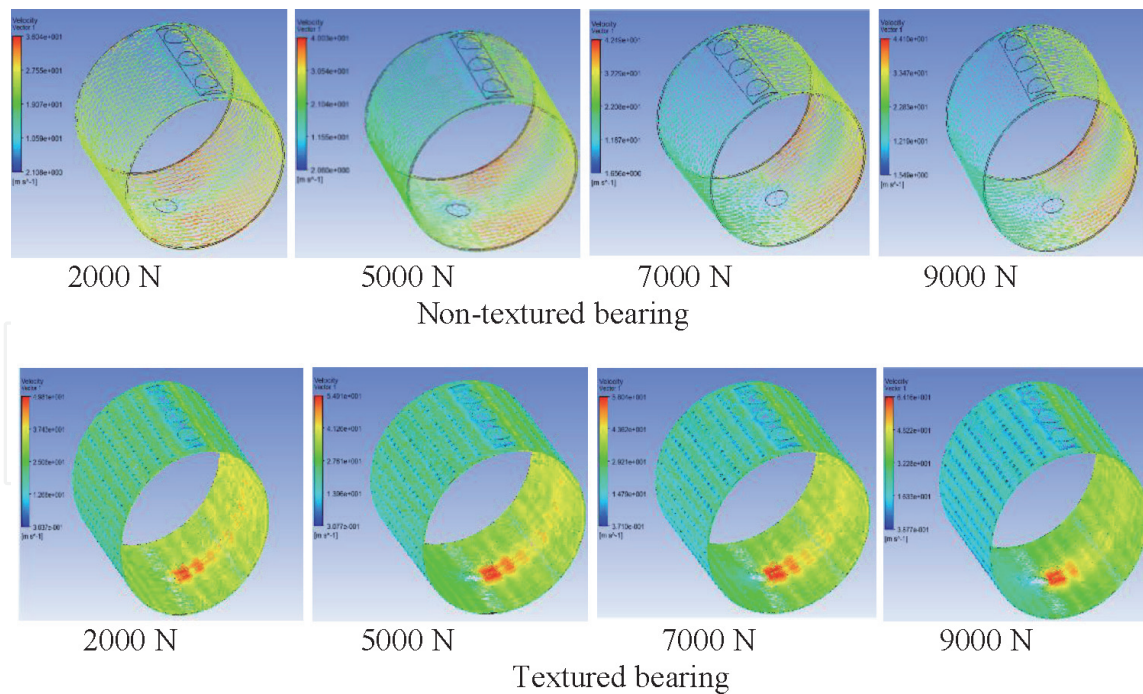
Figure 12.
Velocity evolution for different radial load N = 11,000 rpm.
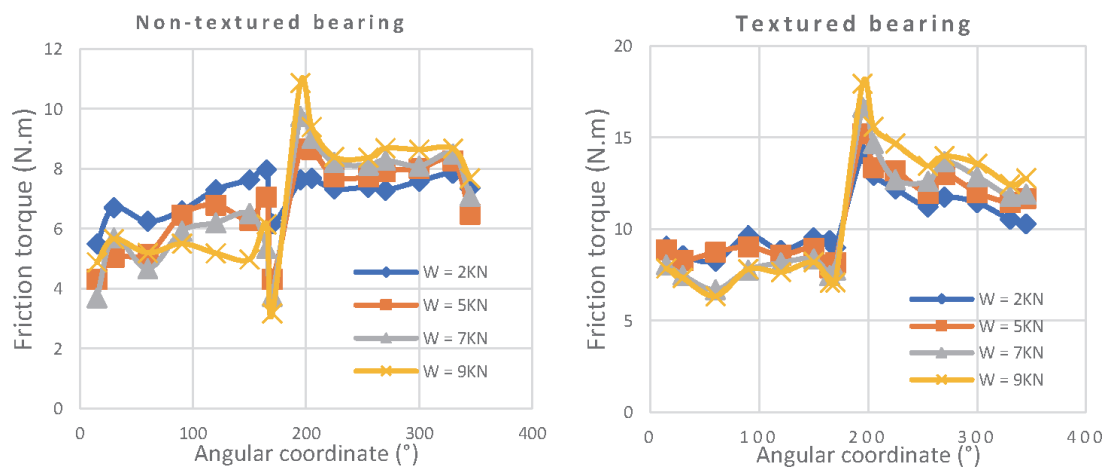

Figure 13.
Friction torque in the median plane for different radial load N = 11,000 rpm (Re = 3622.64 turbulent regime).

The friction torque along the circumference of the textured bearing is illustrated in **Figure 13**. The important values are noted for a radial load of 9000 N, the maximum value of the friction torque is of the order of 17.93 N.m for a textured bearing, and is the order of 10.83 N.m for non-textured bearing. These maximum values are noted in the angular positions at 180° and 195°. The increase in the radial load from 2000 N to 9000 N leads to an increase in the friction torque of 21 per cent and 29 per cent respectively for a textured and non-textured bearing.

7.3 Effect of the shaft rotation speed

7.3.1 Pressure

Figure 14 shows the pressure distribution along the bearing circumference, for four shaft rotation speeds (11,000 rpm, 14,000 rpm 17,000 rpm and 21,000 rpm). The supply conditions used for this numerical analysis are Ta = 40°C and Pa = 0.08 MPa. The radial load is 10,000 N. This rotational speed gives respectively
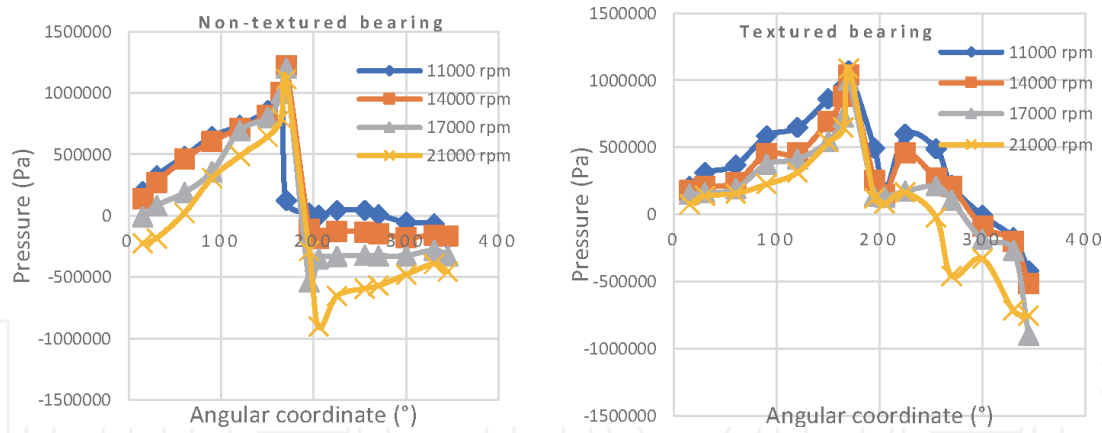
Figure 14.
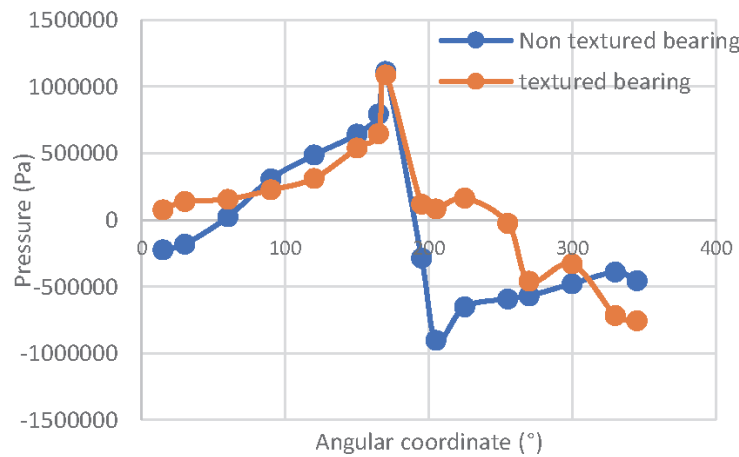*Circumferential pressure for different rotational velocity W = 10 KN (turbulent regime).*

Figure 15.
Circumferential pressure according the angular coordinate of the non- textured and textured bearing W = 10 KN, N = 14,000 rpm (Re = 5187.6 turbulent regime).

a Reynolds number of Re = 3622.64, Re = 4687.53, Re = 5187.6 and Re = 6752.54, which indicates that the regime is turbulent.

The curve clearly shows that the maximum pressure is positioned at angular coordinates from 140° to 160°, while at angular positions between 170° and 200°, the pressure is lower than the supply pressure, which indicates the existence of the rupture zone of the oil film. It can also be said that increasing the rotational speed causes a slight decrease in pressure, this decrease being estimated at 24 per cent. The significant pressure is recorded for a very high rotation speed, which is of the order of 21,000 rpm.

Figure 15 shows the pressure distribution as a function of the angular position for a textured and non-textured bearing for a radial load of 10,000 N and a rotation speed of 14,000 rpm. The curve clearly shows that the pressure distribution along the median plane of the bearing is different in the case of a non-textured bearing and a bearing with a textured surface; the difference is estimated at 8.5 per cent (**Figure 16**).

7.3.2 Fluid flow velocity

Figure 17 illustrates the variation of flow velocity in the circumferential direction of the plain bearing, to a feed temperature of 40°C and feed pressure of 0.08 MPa. The shaft rotational speed varies from 11,000 rpm to 21,000 rpm (Turbulent regime) and a radial load of 10,000 N. The curve shows that the rotational speed leads to an increase in the fluid flow velocity. The increase reached 39 per cent. The flow velocity is significant for a bearing which rotates at a speed of
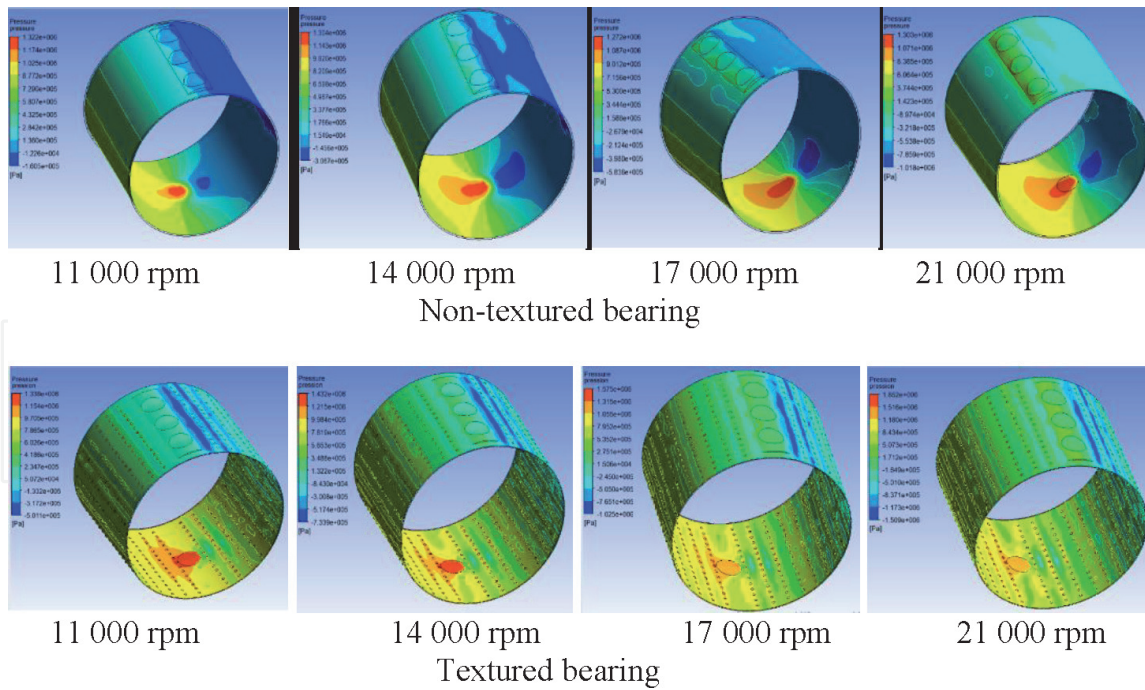
11 000 rpm 14 000 rpm 17 000 rpm 21 000 rpm

Non-textured bearing

11 000 rpm 14 000 rpm 17 000 rpm 21 000 rpm

Textured bearing

Figure 16.
Distribution circumferential of the pressure for differents rotational velocity.

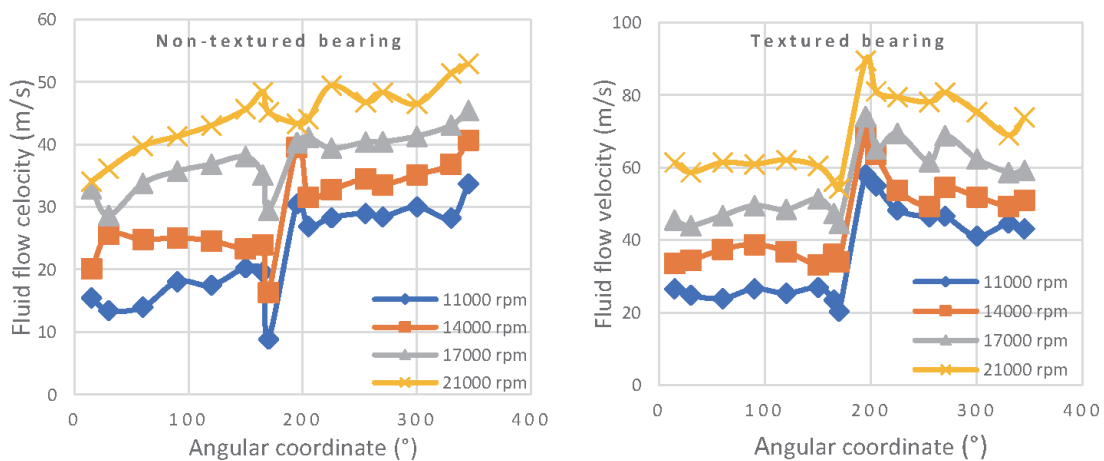**Figure 17.**
Fluid flow velocity evolution according angular position angular for different rotational speed W = 10 KN (turbulent regime).

21,000 rpm (Re = 6752.54), on the other hand it is less important for a rotational speed of 11,000 rpm (Re = 3622.64). The significant value of the fluid flow velocity is noted for a textured plain bearing which is the order of 89.56 m/s. On the other hand, for a non-textured plain bearing, the maximum value of the fluid flow velocity is only of the order of 56.37 m/s.

For the different of the fluid flow velocity (**Figure 18**), has the same variation for the case of plain bearing without texture and a textured plain bearing. This speed takes a maximum value at the angular coordinate of 200° of the bearing. The difference between the fluid flow velocity for a non-textured and textured plain bearing is of the order of 38 per cent (**Figure 19**).

7.3.3 Friction torque

For the evolution of the friction torque as a function of the angular coordinates of the non-textured and textured plain bearing by varying the rotational speed of
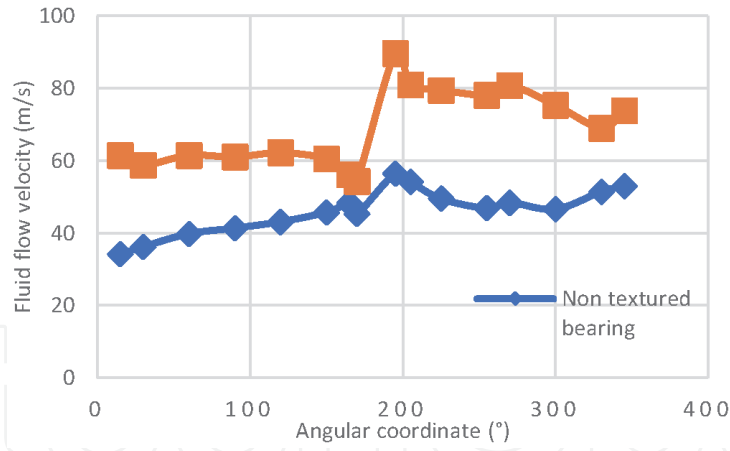
Figure 18.
Fluid flow velocity according angular position of the non-textured and textured bearing W = 10 KN,
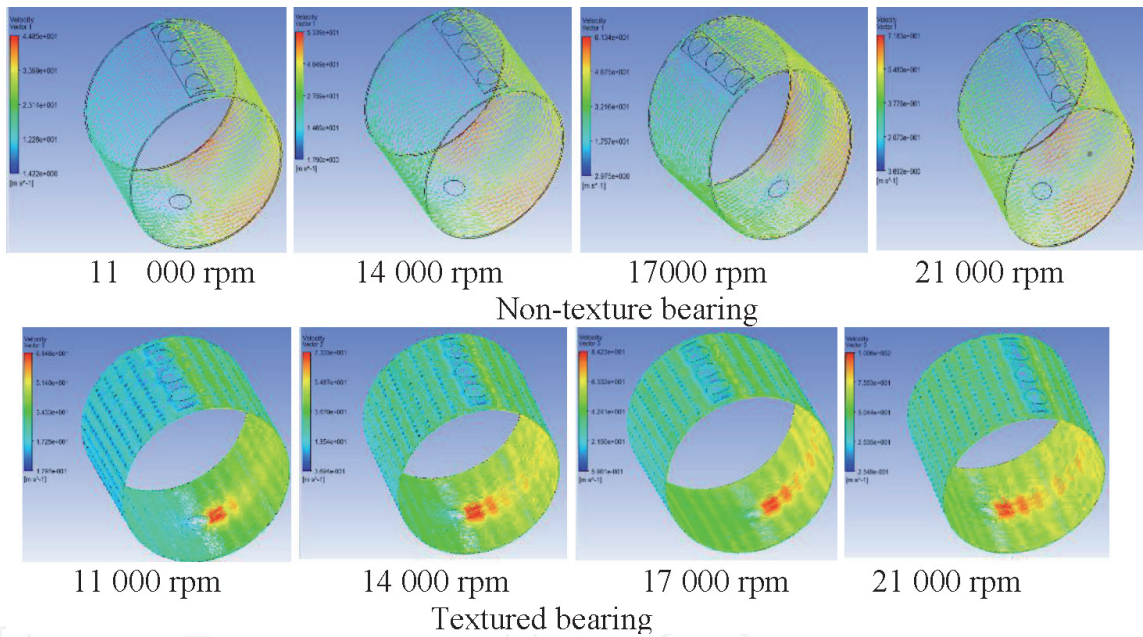*N = 14,000 rpm (Re = 5187.6 turbulent regime).*

Figure 19.
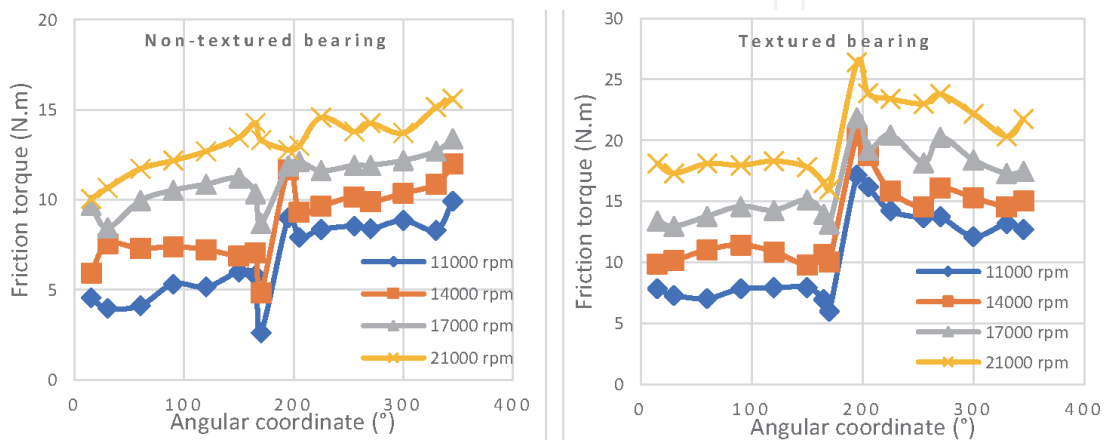*Distribution circumferential of the fluid flow velocity for differents rotational velocity.*

Figure 20.
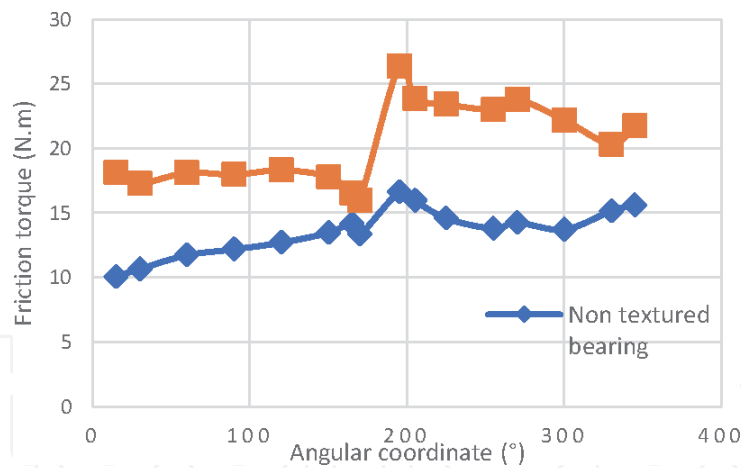*Friction torque in median plane for different rotational speed W = 10 KN (turbulent regime).*

Figure 21.
Friction torque in the median plane of the non-textured and textured bearing W = 10 KN, N = 14,000 tr/min (Re = 5187.6 turbulent regime).

the shaft from 11,000 to 21,000 rpm and for a radial load of 10,000 N, is presented in **Figure 20**. The increasing the rotational speed causes a slight increase in the friction torque, this increase is of the order of 2 per cent. The important values are obtained for a rotational speed of 21,000 rpm; the maximum value of the friction torque is also positioned at the angular coordinate of 200°. The significant value of the friction torque for a non-textured plain bearing is of the order of 16 N.m, on the other hand for a textured plain bearing is 26 N.m.

Figure 21 illustrates the variation of friction torque along the circumferential non-textured and textured plain bearing. The evolution of the friction torque along the angular bearing position has the same shape for the two cases studied, the difference is estimated at 38 per cent at the 200° level.

8. Conclusions

This numerical study presents the evolution of the fluid flow for turbulent regime in hydrodynamic plain bearings with a non-textured and textured surface, in order to improve the hydrodynamic lubrication and tribological performance of plain bearing, using the finite volume method, such as pressure, friction torque and fluid flow velocity.

The results obtained for the textured plain bearing were compared to the non-textured plain bearing, the main conclusions drawn from this study are:

1. The pressure distribution according to the angular position for the textured and non-textured plain bearing for the radial load of 10,000 N and the speed of rotation of 14,000 rpm has the same appearance for the two cases studied; the difference is estimated at 8.5%.

2. The rupture zones of the oil film are observed in several angular positions at 190° and 300° for a plain bearing with textured surface, on the other hand for a plain bearing without texture, the rupture zone is positioned only in the angular position at 190°. This rupture of the oil film is due to the drop in pressure below the supply pressure.

3. The evolution of the friction torque, along the angular position, has the same distribution for the non-textured and the textured plain bearing, the difference is estimated at 38%.

19

4. The flow velocity of the fluid in the plain bearing takes a maximum value at the angular position of 165°. The difference between the flow velocity for a non-textured and textured plain bearing is estimated of 38%.

It should be emphasized, however, that the conclusions we give here are only valid for the cases we have studied, and that they are not independent of the characteristics of the plain bearing and of the lubricant.

The numerical results show that the most significant hydrodynamic characteristics such as pressure, flow velocity of the fluid and friction torque, are significant for the textured plain bearing under rotational velocity of 21,000 rpm and radial load 10,000 N compared to the results obtained for a non-textured plain bearing.

When one is interested in plain bearings operating under severe conditions, that is to say for the turbulent regime, the hydrodynamic pressures sometimes reach several hundred mega Pascal's.

Conflict of interest

The authors declare no conflict of interest.

Nomenclature

B	source term
C	radial clearance
e	eccentricity
L	bearing length
R_S	shaft radius
R_B	bush radius
N	rotational velocity [rpm]
P	pressure [Pa]
r_i	position vector [m]
U	peripheral speed [m/s]
U, v, w	velocity according x, y, z axis [m/s]
W	radial load [N]
Re	Reynolds number
ε	relative eccentricity
ϕ	Flow factor [°]
μ	dynamic viscosity [Pa.s]
μt	turbulent dynamic viscosity [Pa.s]
ω	shaft angular speed [rad/s]
K	turbulence kinetic energy
ρ	density [kg/m³]

Indice

i	Interne
ip	Indice du point d'intégration
s	spécifique
t	théorique
u	utile

Author details

Bendaoud Nadia* and Mehala Kadda
Faculty of Mechanical Engineering, University of the Sciences and Technology of
Oran Mohamed Boudiaf, Oran, Algeria

*Address all correspondence to: nadiamehala@yahoo.fr

IntechOpen

References

[1] Constantinescu, V.N. (1959), "On turbulent lubrication", *Proceedings of the Institution of Mechanical Engineers*, Vol. 173 Nos. 3/8, pp. 881–900. doi.org/10.1243/PIME_PROC_1959_173_068_02

[2] Constantinescu, V.N. (1962), "Analysis of bearings operating in turbulent regime", *ASME Journal of Fluids Engineering*, Vol. 84 No. 1, pp. 139–151. DOI.org/10.1115/1.3657235

[3] Elrod, H.G. and Ng, C.W. (1967), "A theory for turbulent films and its application to bearings", *ASME Journal of Tribology*, Vol. 86, pp. 346–362. DOI.org/10.1115/1.3616989

[4] Ng, C.W. (1964), "Fluid dynamic foundation of turbulent lubrication theory", *ASLE Transactions*, Vol. 7 No. 4, pp. 311–321. DOI/abs/10.1080/05698196408972061

[5] Ng, C.W. and Pan, C.H.T. (1965), "A linearized turbulent lubrication theory", *ASME Transactions Journal of Fluids Engineering*, Vol. 87 No. 3, pp. 675–688. DOI.org/10.1115/1.3650640

[6] Fantinos B., Frêne J., Godet M., (1972), "Reynolds equation in viscous film theory", Trans, ASME, Journal of Lubrication Technology, vol. 94, n°3, pp: 287–288. DOI.org/10.1115/1.3451713

[7] Braunetiere, N. (2005), "A modified turbulence model for low Reynolds numbers: application to hydrostatic seals", *ASME Transactions Journal of Tribology*, Vol. 127 No. 1, pp. 130–140. DOI: 10.1115/1.1829721

[8] Solghar A.A and Nassab G., (2013), "Numerical analysis of turbulent lubrication in plain full journal bearings", Industrial Lubrication and Tribology, Vol.65 N°2, pp: 91–99. DOI/10.1108/00368791311303456

[9] Spalart, P.R., Jou, W.H., Strelets, M., and Allmaras, S.R., (1997), "Comments on the feasibility of LES for wings, aud on a hybrid RANS/LES approach." lst AFOSR Int. Conf. On DNS/LES, Aug.4–8. https://www.cobaltcfd.com/pdfs/DES97.pdf

[10] Krupka, I., Hartl, M., Zimmerman, M., Houska, P. and Jang, S., Effect of surface texturing on elastohydrodynamically lubricated contact under transient speed conditions, *Tribology International*, vol. **44**, no.10, pp. 1144–1150, 2011. DOI: 10.1016/j.triboint.2011.05.005

[11] Tala-Ighil, N., Fillon M. and Maspeyrot, P., Effect of textured area on the performances of a hydrodynamic journal bearing, *Tribology international*, vol. **44**, no. 3, pp. 211–219, 2011. DOI: 10.1016/j.triboint.2010.10.003

[12] Pratibha, S. and Chandreshkumar, R., Effect of Bearing Surface Texture on Journal Bearing Pressure, *International Journal of Science and Research (IJSR)*, vol. **3**, no. 6, pp. 2223–2226, 2014. paper_id=2014693

[13] Zhang, Y.L., Zhang, X.G. and Matsoukas, G. Numerical study of surface texturing for improving tribological properties of ultra-high molecular weight polyethylene, *Science direct Biosurface and Biotribology*, vol. **1**, pp.270–277, 2015. DOI.org/10.1016/j.bsbt.2015.11.003

[14] Uddin, M.S. and Liu, Y.W, Design and optimization of a new geometric texture shape for the enhancement of hydrodynamic lubrication performance of parallel slider surfaces, *Science direct, Biosurface and Biotribology* vol. **2**, pp. 59–69, 2016. DOI.org/10.1016/j.bsbt.2016.05.002

[15] Hamdavi, S., Ya, H.H. and Rao, T. V. V. L. N. Effect of surface texturing on hydrodynamic performance of journal bearings, ARPN Journal of Engineering

and Applied Sciences, vol. **11**, no.1, pp.172–176, 2016. https://www.resea rchgate.net/profile/T_V_V_L_N_Rao/ publication/293820391

[16] Sedlaček, M., Podgornik, B., Ramalho, A. and Česnik, D. Influence of geometry and the sequence of surface texturing process on tribological properties, *Tribology international*, vol. **115**, pp. 268–273, 2017. DOI.org/ 10.1016/j.triboint.2017.06.001

[17] Wang, J., Zhang, J.,Lin, J. and Liang, M., Study on Lubrication Performance of Journal Bearing with Multiple Texture Distributions, *Applied Sciences*, vol. **224**, no.8, pp. 1–13, 2018. DOI.org/ 10.3390/app8020244

[18] Ji, J.-H., Guan, C.-W. Fu, Y.-H. (2018) Effect of Micro-Dimples on Hydrodynamic Lubrication of Textured Sinusoidal Roughness Surfaces, *Chinese Journal of Mechanical Engineering*, vol. **31**, art no. 67, 2018. DOI: 10.1186/ s10033-018-0272-z

[19] Manser B., Belaidi I., Hamrani A., Khalladi S., Bakir F., Performance of hydrodynamic journal bearing under the combined influence of textured surface and journal misalignment: A numerical survey, *Comptes rendus Mécanique*, vol **347**, no. 2, pp.141–165, 2019. DOI : 10.1016/j.crme.2018.11.002

[20] ANSYS-CFX "Documentations Solver Theory",(2009).